Research Square

Preprints are preliminary reports that have not undergone peer review.
They should not be considered conclusive, used to inform clinical practice,
or referenced by the media as validated information.

Confinement magnitude dominates cross-sectional geometry in hydrophobic sphere water entry

Daren Watson

dwatson@floridapoly.edu

Florida Polytechnic University https://orcid.org/0000-0002-3371-2843

Zamar Joseph

Florida Polytechnic University https://orcid.org/0009-0007-3782-0714

Adrian Santos

Florida Polytechnic University https://orcid.org/0009-0003-3029-6113

Research Article

Keywords: cavities, drag, pipes, splash, wall effects

Posted Date: September 15th, 2026

DOI: https://doi.org/10.21203/rs.3.rs-11026844/v1

License: This work is licensed under a Creative Commons Attribution 4.0 International License.
Read Full License

Additional Declarations: The authors declare no competing interests.

Confinement magnitude dominates cross-sectional geometry in hydrophobic sphere water entry

Daren A. Watson[a,*], Zamar C. Joseph[a], & Adrian A. Santos[a]

[a]Mechanical Engineering Department, Florida Polytechnic University, Lakeland, FL, 33805, USA

*Corresponding author: dwatson@floridapoly.edu

Abstract

Water entry dynamics is strongly modified by nearby solid boundaries, yet it remains unclear whether confined entry is governed primarily by the characteristic magnitude of confinement or by the detailed geometry of the surrounding boundary. We experimentally investigate water entry of hydrophobic spheres through semi-infinite pipes having circular, triangular, square and hexagonal cross-sections for Froude numbers and normalized pipe diameters in the ranges of $21 - 97$ and $2 - 7.13$, respectively. Splash crown formation, cavity dynamics, and hydrodynamic loading are quantified and compared with unbounded water entry. Increasing confinement magnitude produces systematic changes in all measured responses, whereas differences among cross-sectional geometries diminish as normalized pipe diameter increases. Geometry-dependent effects are strongest under severe confinement, where spatial variations in wall proximity produce pronounced changes in cavity morphology and promote multiple pinch-off locations. Hydrodynamic loading exhibits the same hierarchy, with confined spheres experiencing greater deceleration and drag than under unbounded water entry. We show that the inscribed diameter used to characterize the circular and regular polygonal pipes is also their common hydraulic diameter, providing a physical basis for comparison using a single leading-order confinement scale. Results identify pipe diameter as the principal geometric control of the confined behavior over the present parameter range, while cross-sectional shape acts as an increasingly important correction as the sphere approaches the surrounding boundary.

Keywords: [cavities, drag, pipes, splash, wall effects]

1 Introduction

The extensive body of research on the water entry of solid projectiles impacting deep liquid pools has broad relevance to practical phenomena, including toilet dynamics, sports engineering, animal locomotion, missile water entry, sea-surface landing, and underwater transport [1–6]. Accordingly, water entry has remained a focal topic in fluid dynamics, with previous investigations primarily examining the effects of surface roughness [7–11], impact velocity [10,12], and projectile geometry [13–15]. This sustained interest is unsurprising given the rich body of literature established since the seminal investigations of Worthington [16–18] in the late nineteenth century. Nevertheless, the vast majority of water entry studies have considered unbounded fluid domains in which the influence of nearby solid boundaries, commonly referred to as "wall effects," is negligible [12]. A limited number of studies have instead examined water entry in the presence of nearby boundaries, demonstrating that confinement can substantially modify projectile trajectories, cavity morphology, and hydrodynamic forces. Ern and Brosse [19], for example, investigated the water entry of two identical disks falling side by side at moderate Reynolds numbers ($\mathrm{Re} = 100 - 300$) and identified lateral repulsive forces when the disk centers were separated by less than 4.5 diameters. At larger separation distances, disks maintained straight-line trajectories as lateral interaction diminished. Subsequent numerical investigations by Lu *et al.* [20] and Wang *et al.* [21] corroborated the presence of lateral repulsive forces between closely spaced ($\lesssim 3$ diameters) parallel projectiles and demonstrated that confinement between neighboring projectiles can produce cavity asymmetry, trajectory instability, and increased drag relative to an isolated projectile. Experimental investigations have similarly demonstrated that nearby projectiles can strongly influence cavity dynamics. Akbarzadeh *et al.* [5] showed that, at sufficiently small separation distances ($\lesssim 5$ diameters), deep-seal cavities generated by parallel hydrophobic spheres become asymmetric, with pinch-off occurring at a single location. Using a hydrophilic-hydrophobic sphere pairing, Akbarzadeh *et al.* [22] subsequently demonstrated the emergence of

multiple pinch-off locations during the simultaneous descent of proximal spheres. The formation of multiple pinch-off points was attributed to the migration of vortex rings generated in the wake of the descending hydrophilic sphere, which produces indentations along the cavity walls that subsequently grow radially. The influence of a stationary solid boundary has also been examined. Zeng *et al.*[23] numerically investigated a rigid sphere translating tangentially near a flat wall at separation distances less than two sphere diameters. Their results revealed a lift force directed away from the wall, distortion of the cavity along the wall-facing side of the sphere, and increased drag associated with viscous interactions in the confined region. These findings were subsequently confirmed experimentally by Mansoor *et al.*[24], who quantified the influence of wall proximity on cavity pinch-off location and time, and established a useful sphere-to-tank diameter threshold $\sim 1/16$, beyond which measurable wall effects become negligible. Most recently, Watson *et al.*[25] investigated the influence of normalized pipe diameter on splash dynamics and hydrodynamic loading experienced by hydrophobic spheres traversing semi-infinite circular pipes. Their results demonstrated that decreasing normalized pipe diameter produces higher splash crowns, smaller cavities, and slower sphere descent, highlighting the importance of radial confinement in governing projectile water entry[25].

Although these studies establish that nearby boundaries can fundamentally modify water entry dynamics, the coupled contributions of confinement magnitude and boundary geometry remain unclear. Previous investigations of wall effects have primarily considered planar boundaries, circular pipes, or arrangements of parallel projectiles, for which confinement can often be characterized by a single wall proximity or diameter parameter. In our study, noncircular pipes introduce spatially varying wall proximity around the descending sphere and therefore provide a means of independently examining the effects of confinement magnitude and cross-sectional shape. An important unresolved question is whether this geometric complexity produces a substantial modification of water entry dynamics beyond that associated with wall proximity. Thus, the key question is the extent to which, under comparable sphere-to-wall confinement, cross-sectional geometry influences splash crown formation, cavity dynamics, and hydrodynamic loading, as opposed to these metrics being primarily governed by confinement magnitude. Resolving this distinction is important for determining whether cross-sectional shape must be treated as an independent control parameter when describing water entry in confined conduits.

Here, we experimentally investigate hydrophobic sphere water entry through semi-infinite pipes having circular, triangular, square, and hexagonal cross-sections, as shown in **Fig.1**a. Spheres with diameters $D_\mathrm{s} = 1.60$ and 1.90 cm are released from heights $h = 20 - 75$ cm, corresponding to a Froude number range of $\mathrm{Fr} = U^2/gD_\mathrm{s} = 21 - 97$, where $U \approx (2gh)^{1/2}$ is the sphere impact velocity and $g = 9.81$ ms^{-2} is the acceleration due to gravity. Streamwise pipe enclosures extend to the floor of the liquid pool, such that descending spheres are confined for the entire duration of water entry[25]. Pipe geometries are tested at comparable normalized inscribed diameters D_p, enabling the influence of confinement magnitude to be compared directly with that of cross-sectional shape. We quantify the resulting influence of our confinement parameters on splash crown width λ, splash crown height γ, cavity depth κ, and hydrodynamic drag coefficient C_D. Measurements obtained in an unbounded pool $D_\mathrm{p} = \infty$ provide a baseline for quantifying the magnitude of confinement effects. By comparing multiple cross-sectional geometries at equivalent normalized pipe diameters, we assess whether pipe diameter or cross-sectional shape provides the stronger control over water entry dynamics. This approach shifts the emphasis from simply characterizing noncircular confinement to determining the relative importance of confinement magnitude and geometric form in governing the response of a confined water entry system.

Beyond the present experiments, passive projectile transport through fluid-filled pipes is encountered in numerous engineering systems. One example is the falling-ball viscometer[26], which determines fluid viscosity from the descent of a sphere through a confined liquid column. Related transport processes arise in sampling devices, underwater deployment systems, and industrial piping networks, where pipe dimensions and cross-sectional geometry can vary substantially[26–28]. By quantifying the effects of confinement on splash crown formation, cavity dynamics, and hydrodynamic loading, the present work provides insight into bounded projectile transport and, in particular, clarifies the relative roles of confinement magnitude and cross-sectional geometry. These findings provide a basis for assessing passive underwater transport through fluid-filled conduits with diverse cross-sectional shapes. We present our experimental methods for confinement properties, sphere surface treatment, and water entry experiments in Section 2. Results and theoretical considerations are presented in Section 3, and the implications of this work are discussed in Section 4. We conclude the study in Section 5.

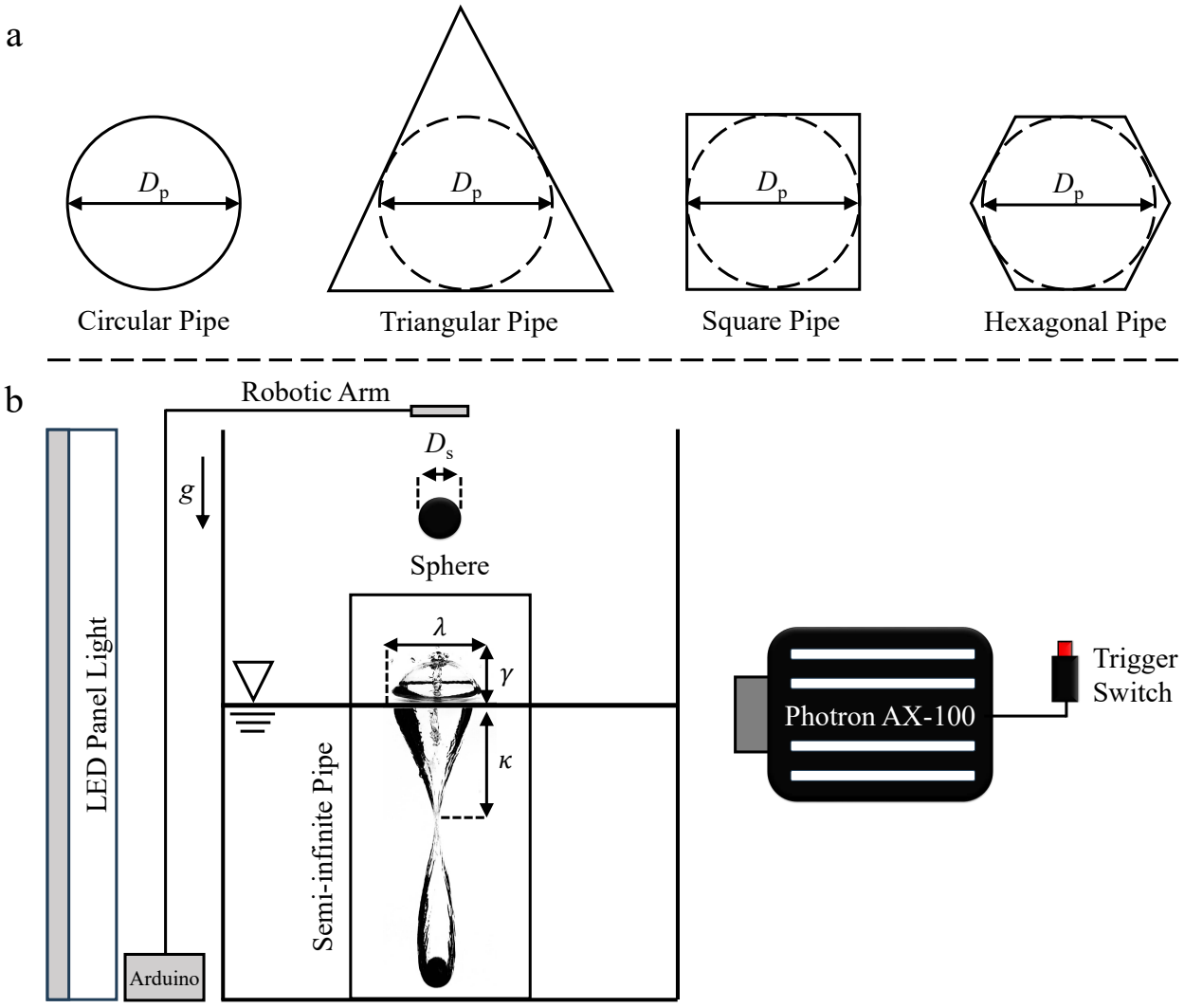


Figure 1: **(a)** Pipe geometries with inscribed diameters D_p. **(b)** Schematic of experimental setup with semi-infinite pipe resting inside the aquarium. Photron Mini AX-100 high-speed video camera captures frontal view of impacts with LED panel lights positioned behind the aquarium. Optional BNC trigger switch complements manual camera controls in video recording software (Photron FASTCAM Viewer). Switch-controlled robotic arm powered by an Arduino Uno grips and releases spheres. Splash crown width and height are denoted by λ and γ, respectively, while cavity depth is denoted by κ.

2 Methods

2.1 Confinement properties

Two smooth stainless-steel spheres with masses of $m_s = 16.60$ and 28.60 g and diameters of $D_s = 1.60$ and 1.90 cm, respectively, are released into a 122-L, 45-cm deep aquarium filled to 75% capacity with tap water[25]. Similar to protocols established by Watson *et al.*[25], the aquarium's water depth is selected to ensure that cavity pinch-off occurs before spheres contact the aquarium floor over the range of sphere release heights h for unbounded entry conditions. These conditions are known to yield the geometric limit of cavity depths[12], while providing sufficient spatial separation between cavity pinch-off and the aquarium floor to reduce wall effects associated with a finite liquid depth[29]. Throughout each experiment, spheres descend within semi-infinite pipes, whose characteristic dimensions are chosen to produce confinement ratios comparable to those

commonly employed in studies of moving and stationary boundary effects[5,19–24]. These confinement ratios, calculated as the normalized pipe diameters, are in the range $\chi = D_\mathrm{p}/D_\mathrm{s} = 2 - 7.13$ and are tabulated in **Table 1**. Values for χ closely align with previously tested values for circular pipes[25]. We therefore denote the strength of confinement, commonly referred to as confinement magnitude, as $\mathcal{C} = 1/\chi$. Pipes are fabricated from optically transparent acrylic to facilitate unobstructed visualization with a high-speed camera and have a wall thickness of 0.2 cm and a length of 46 cm. Selected geometries systematically vary cross-sectional confinement while maintaining a consistent vertical extent and inscribed diameter D_p, thereby enabling direct examination of the effects of noncircularity and spatially varying wall proximity on splash and cavity dynamics during water entry. For convenience, we introduce a variable, denoted by $\mathcal{G}$, to represent pipe cross-sectional geometry such that

$$\mathcal{G} = \begin{cases} n = 3, & \text{triangular,} \\ n = 4, & \text{square,} \\ n = 6, & \text{hexagonal,} \\ n \to \infty & \text{circular.} \end{cases} \tag{1}$$

where n is the number of sides corresponding to pipe shape.

Table 1: Normalized pipe diameters χ derived from the diameters of semi-infinite pipes D_p and spheres D_s on test. Pipe diameters D_p correspond to the inscribed (wall-to-wall) diameters common across different geometries.

Pipe diameter, D_p	Normalized pipe diameter, $\chi = D_\mathrm{p}/D_\mathrm{s}$	
cm	$D_{\mathrm{s},1} = 1.60$ cm	$D_{\mathrm{s},2} = 1.90$ cm
3.80	2.38	2.00
7.60	4.75	4.00
11.40	7.13	6.00
∞ (Unbounded)	∞	∞

2.2 Sphere surface treatment

To make spheres hydrophobic, we coat their surfaces with Rust-Oleum NeverWet. Each sphere is sprayed twice with the base coat and allowed to dry for 30 min before two applications of the top coat[25]. During coating, the spray nozzle is maintained approximately 30 cm from the spheres' surface. Coated spheres are allowed to cure for at least 12 h before use in experiments. The equilibrium contact angle of water on coated spheres is $\theta_\mathrm{e} = 113^\circ \pm 7^\circ$ ($N = 12$), measured photographically by depositing water onto the spheres' surface using a syringe[25]. In between impact trials, spheres are allowed to dry, thereby minimizing the influence of residual water on subsequent tests.[25].

2.3 Water entry experiments

Coated spheres are positioned above the openings of pipes using a custom-built, 3D-printed robotic arm that enables rapid release from drop heights in the range $h = 20 - 75$ cm. The release mechanism ensures that spheres undergo purely vertical, irrotational free fall prior to water entry[25]. A schematic of the experimental configuration is shown in **Fig.1**b. The switch-controlled robotic arm, powered by an Arduino Uno and interfaced with a computer, provides an enhanced release mechanism relative to established water entry protocols that commonly employ electromagnets[12] or manually operated reclining levers[2]. For each experimental condition, three replicate trials are conducted to account for experimental variability, particularly given the sensitivity of splash metrics to small deviations between nominally identical trials[25]. Mean

and standard deviation σ_{std} values are calculated for each measured quantity, with error bars included in plots where appropriate to characterize experimental reproducibility. Water entry events are recorded using a Photron Mini AX-100 high-speed video camera operating at 2000 frames per second with a 120-mm Nikon lens. Geometric measurements and position track data are extracted from videos using Open-Source Physics Tracker, and sphere kinematics evaluated using MATLAB®.

2.4 Geometric and dynamic scaling

Hydraulic diameter

The present experiments seek to distinguish the characteristic magnitude of confinement $\mathcal{C}$ from effects associated with the detailed cross-sectional geometry $\mathcal{G}$. We therefore first consider geometric scales common to circular and regular polygonal pipes shown in **Fig.1**a. For a regular $n-$sided polygon circumscribed about a circle of diameter D_{p}, cross-sectional area A_{p} and perimeter P_{p} are

$$A_{\text{p}} = \frac{nD_{\text{p}}^2}{4} \tan\left(\frac{\pi}{n}\right), \tag{2}$$

and

$$P_{\text{p}} = nD_{\text{p}} \tan\left(\frac{\pi}{n}\right), \tag{3}$$

respectively. The corresponding hydraulic diameter D_{h} is therefore

$$D_{\text{h}} = \frac{4A_{\text{p}}}{P_{\text{p}}} = D_{\text{p}}. \tag{4}$$

The same equality follows trivially for circular pipes, for which $A_{\text{p}} = \pi D_{\text{p}}^2/4$ and $P_{\text{p}} = \pi D_{\text{p}}$. Thus, despite substantial differences in cross-sectional shape, all pipes having a common inscribed diameter D_{p} also possess the same hydraulic diameter D_{h}. Normalized pipe diameter $\chi = D_{\text{p}}/D_{\text{s}} = D_{\text{h}}/D_{\text{s}}$ therefore provides a common characteristic measure of geometric confinement for all shapes considered here. Given $\mathcal{C} = 1/\chi$, stronger confinement corresponds to increasing $\mathcal{C}$, or equivalently decreasing χ.

Area blockage ratio

Equal hydraulic diameter does not, however, imply equal cross-sectional fluid area. A second geometric measure is therefore provided by the area blockage ratio,

$$\beta = \frac{A_{\text{s}}}{A_{\text{p}}}, \tag{5}$$

where $A_{\text{s}} = \pi D_{\text{s}}^2/4$ is the projected sphere area. For regular polygonal pipes,

$$\beta = \frac{\pi}{n \tan(\pi/n)} \left(\frac{D_{\text{s}}}{D_{\text{p}}}\right)^2, \tag{6}$$

whereas for circular pipes

$$\beta = \left(\frac{D_{\text{s}}}{D_{\text{p}}}\right)^2. \tag{7}$$

Hence, two pipes having identical χ possess identical hydraulic confinement scales but different available cross-sectional areas. Thus, changes to water entry dynamics observed among pipe shapes at fixed χ may be interpreted as deviations from the influence associated with their common hydraulic diameter D_{h}. Normalized hydraulic diameters $D_{\text{h}}/D_{\text{p}}$ and area blockage ratios β corresponding to tested cross-sectional geometries $\mathcal{G}$ are tabulated in **Table 2**. Although pipes having the same inscribed diameters D_{p} possess identical hydraulic diameters D_{h}, their normalized cross-sectional areas $A_{\text{p}}/D_{\text{p}}^2$ differ, providing a shape-dependent measure of the fluid area available around the descending sphere.

Table 2: Normalized hydraulic diameters and area blockage ratios corresponding to tested cross-sectional geometries.

Pipe geometry, $\mathcal{G}$	Sides, n	Normalized area ratio, $A_\mathrm{p}/D_\mathrm{p}^2$	Normalized hydraulic diameter, $D_\mathrm{h}/D_\mathrm{p}$	Area blockage ratio, β
Circular	–	$\pi/4$	1	$\mathcal{C}^2$
Triangular	3	$3\sqrt{3}/4$	1	$\pi\mathcal{C}^2/3\sqrt{3}$
Square	4	1	1	$\pi\mathcal{C}^2/4$
Hexagonal	6	$3/(2\sqrt{3})$	1	$\pi\mathcal{C}^2\sqrt{3}/6$

A simple continuity argument provides a physical basis for the increasing sensitivity to confinement. During sphere descent, the characteristic volumetric displacement rate Q_s scales as

$$Q_\mathrm{s} \sim U D_\mathrm{s}^2. \tag{8}$$

The displaced liquid must be redirected through the fluid area A_f surrounding the sphere, whose characteristic magnitude is $A_\mathrm{f} \sim A_\mathrm{p} - A_\mathrm{s}$. Consequently, a characteristic velocity U_f associated with confinement-induced fluid redistribution may be estimated as $U_\mathrm{f} = Q_\mathrm{s}/A_\mathrm{f}$ such that

$$U_\mathrm{f} \sim \frac{U D_\mathrm{s}^2}{A_\mathrm{p} - A_\mathrm{s}}. \tag{9}$$

Considering the area blockage ratio,

$$\frac{U_\mathrm{f}}{U} \sim \frac{\beta}{1-\beta}, \tag{10}$$

up to a geometry-dependent factor of order unity associated with the detailed three-dimensional flow around the sphere. Eq.(10) predicts rapidly increasing fluid-redistribution velocities as the available flow area decreases. An associated inertial pressure scale is

$$\rho U_\mathrm{f}^2 \sim \rho U^2 \left(\frac{\beta}{1-\beta}\right)^2, \tag{11}$$

where $\rho = 999$ kg/m^3 is the density of water, suggesting a direct connection between geometric blockage, free-surface deformation and increased hydrodynamic resistance. Cross-sectional geometry $\mathcal{G}$ is expected to enter primarily through the nonuniform spatial distribution of the available flow area and wall distance, effects that become increasingly important as the sphere approaches the pipe boundary.

Governing parameters

In general, normalized water entry dynamics may be expressed as

$$\left\{\frac{\lambda}{D_\mathrm{s}}, \frac{\gamma}{D_\mathrm{s}}, \frac{\kappa}{D_\mathrm{s}}, C_\mathrm{D}\right\} = f\left(\mathrm{Fr}, \mathrm{Re}, \mathrm{We}, \mathrm{Bo}, \mathcal{C}, \mathcal{G}, \theta_\mathrm{e}, \frac{\rho_\mathrm{s}}{\rho}\right), \tag{12}$$

where Reynolds number $\mathrm{Re} = \rho U D_\mathrm{s}/\mu$, Weber number $\mathrm{We} = \rho U^2 D_\mathrm{s}/\sigma$, and Bond number $Bo = \rho g D_\mathrm{s}^2/\sigma$. Here, $\mu = 8.90 \times 10^{-4}$ Pa·s and $\sigma = 72$ mN/m are the dynamic viscosity and surface tension of water, respectively, and ρ_s is the density of the sphere. Since the working fluid, sphere material, and surface treatment are fixed, and sphere diameter varies over a restricted range, experiments are designed primarily to examine the dependence on Fr, $\mathcal{C}$, and $\mathcal{G}$. The central hypothesis tested below is therefore that the leading-order response can be conceptually written as

$$\Phi = f\left(\mathrm{Fr}, \mathcal{C}\right) + \delta_\mathcal{G}, \tag{13}$$

where Φ denotes a normalized splash, cavity or loading measure and $\delta_{\mathcal{G}}$ represents the geometry-dependent departure from results established by the characteristic confinement scale. Experiments determine both the validity of this hierarchy and the confinement range over which $\delta_{\mathcal{G}}$ becomes dynamically significant.

3 Results

We now examine whether water entry can be organized primarily by confinement magnitude $\mathcal{C}$, and identify conditions under which cross-sectional geometry $\mathcal{G}$ produces measurable departures from this leading behavior. Results are considered sequentially through splash crown formation, cavity dynamics, and hydrodynamic loading, thereby spanning the principal morphological and dynamical manifestations of confinement.

3.1 Confinement magnitude dominates splash crown formation

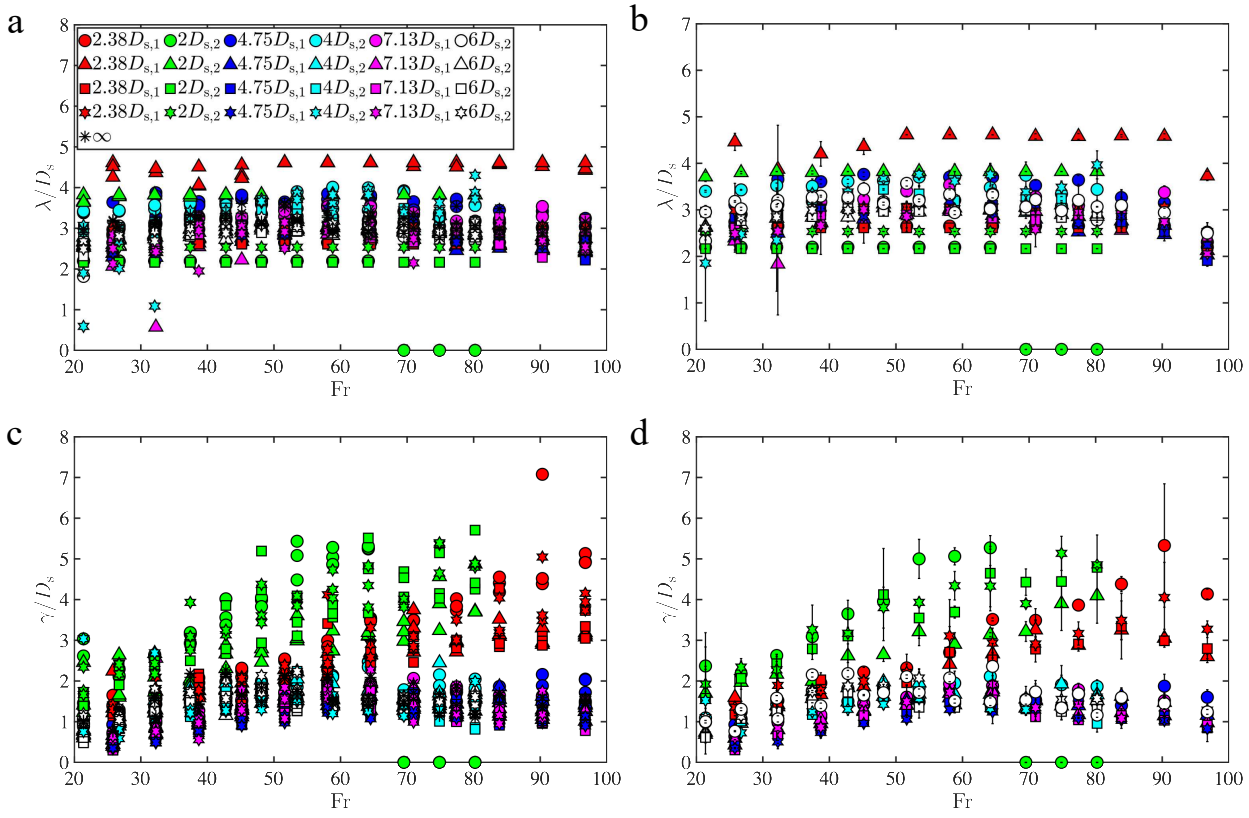


Figure 2: Aggregated plots of normalized splash crown widths λ/D_s showing **(a)** replicate tests and **(b)** average values with error bars vs Froude number. Aggregated plots of normalized splash crown heights γ/D_s showing **(c)** replicate tests and **(d)** average values with error bars vs Froude number. Marker shapes visually denote tested cross-sectional geometries $\mathcal{G}$. Mean, standard deviation, and curve fitting values corresponding to linear and best fit predictions are tabulated in **Table 3** and **Table 4**, respectively.

We plot normalized splash crown widths λ/D_s and heights γ/D_s as functions of Froude number for circular, triangular, square, and hexagonal pipe geometries as shown in **Fig.2**a-d. Across the tested experimental conditions, both splash crown dimensions exhibit a systematic dependence on confinement magnitude, with the largest departures from unbounded results occurring at the smallest normalized pipe diameters. For the unbounded entry condition $\chi = \infty$, mean normalized splash crown widths λ/D_s are 3.24 and 3.08 for the 1.60− and 1.90−cm spheres, respectively. Under finite confinement (**Fig.3**), splash crown dimensions vary with cross-sectional geometry, particularly at $\chi = 2$. This normalized pipe diameter produces mean

values for λ/D_s of 1.65, 3.81, 2.17, and 2.54 for the circular, triangular, square, and hexagonal pipes, respectively. Increasing χ results in more closely grouped splash crown widths, with mean values corresponding to $\chi = 4 - 7.13$ generally falling in the range $\lambda/D_s = 2.7 - 3.5$. These observations, together with the low correlation values R^2 reported in **Table 3** for the scaling relationship $\lambda/D_s \sim Fr^{\zeta}$, are consistent with the theoretical considerations of Watson *et al.*[25], who established that $\lambda \sim D_s$ for the unbounded entry condition, whereas $\lambda \sim D_p$ as $\chi \to 0$. Here, ζ denotes the best fit exponent. Standard deviations for most experimental conditions, typically $\sigma_{std} < 0.5$, further indicate good repeatability in the measured splash crown widths.

Table 3: Mean, standard deviation, and curve fitting correlation values for normalized splash crown widths λ/D_s with respect to Froude number ($N = 36$). Entries where a fit could not be meaningfully obtained are left blank.

Pipe geometry, $\mathcal{G}$	Normalized pipe diameter, χ	Mean	Standard dev., σ_{std}	Best fit R^2, $\zeta = 1$	Best fit exponent, ζ
Circular	2.00	1.65	0.97	0.57	-0.68
	2.38	2.65	0.00	–	–
	4.00	3.54	0.22	0.01	0.02
	4.75	3.48	0.31	0.11	-0.04
	6.00	3.02	0.29	0.05	0.08
	7.13	3.18	0.26	–	0.03
Triangular	2.00	3.81	0.04	0.22	0.01
	2.38	4.46	0.33	0.15	0.07
	4.00	2.94	0.19	0.29	0.10
	4.75	2.69	0.23	–	0.01
	6.00	2.89	0.15	0.38	0.09
	7.13	2.66	0.43	0.08	0.13
Square	2.00	2.17	0.00	–	–
	2.38	2.61	0.01	0.07	–
	4.00	3.18	0.18	0.04	0.04
	4.75	2.83	0.25	0.43	-0.11
	6.00	2.90	0.16	0.24	0.08
	7.13	2.87	0.19	–	0.02
Hexagonal	2.00	2.54	0.00	–	–
	2.38	3.05	0.03	0.15	0.01
	4.00	3.30	0.77	0.46	0.41
	4.75	2.82	0.24	0.02	0.05
	6.00	2.98	0.18	0.30	0.09
	7.13	2.78	0.31	0.02	0.06
∞ ($D_s = 1.60$ cm)	∞	3.24	0.22	0.20	-0.05
∞ ($D_s = 1.90$ cm)	∞	3.08	0.14	0.02	–

Table 4: Mean, standard deviation, and curve fitting correlation values for normalized splash crown heights γ/D_s with respect to Froude number ($N = 36$).

Pipe geometry, $\mathcal{G}$	Normalized pipe diameter, χ	Mean	Standard dev., σ_{std}	Best fit R^2, $\zeta = 1$	Best fit exponent, ζ
Circular	2.00	2.77	1.92	0.09	-0.22
	2.38	3.15	1.34	0.88	1.12
	4.00	1.64	0.39	0.43	0.41
	4.75	1.50	0.36	0.53	0.45
	6.00	1.49	0.25	0.02	0.10
	7.13	1.46	0.39	0.31	0.39
Triangular	2.00	2.80	0.82	0.75	0.67
	2.38	2.45	0.71	0.79	0.67
	4.00	1.60	0.40	0.32	0.37
	4.75	1.34	0.38	0.44	0.48
	6.00	1.37	0.31	0.28	0.32
	7.13	1.26	0.43	0.05	0.23
Square	2.00	3.47	1.15	0.75	0.74
	2.38	2.40	0.78	0.79	0.76
	4.00	1.27	0.34	0.10	0.25
	4.75	1.12	0.35	0.27	0.43
	6.00	1.32	0.31	0.10	0.22
	7.13	1.09	0.39	0.15	0.38
Hexagonal	2.00	3.61	1.04	0.84	0.69
	2.38	2.74	0.92	0.80	0.81
	4.00	1.36	0.47	0.02	0.13
	4.75	0.97	0.30	0.38	0.49
	6.00	1.59	0.30	0.07	0.17
	7.13	1.31	0.43	0.20	0.40
∞ ($D_s = 1.60$ cm)	∞	1.62	0.46	0.11	0.27
∞ ($D_s = 1.90$ cm)	∞	1.56	0.36	0.01	0.01

The influence of confinement magnitude is more pronounced for normalized splash crown heights γ/D_s than for widths λ/D_s . For the unbounded entry configuration $\chi = \infty$, mean normalized splash crown heights γ/D_s are 1.62 for the 1.60−cm sphere and 1.56 for the 1.90−cm sphere, as tabulated in **Table 4**. For $\chi = 2$, these values increase to 2.77, 2.80, 3.47, and 3.61 for circular, triangular, square, and hexagonal geometries, respectively. Increasing normalized pipe diameter to $\chi = 4$ substantially reduces splash crown height, yielding mean values of 1.64, 1.60, 1.27, and 1.36 for the four geometries, respectively. At larger normalized pipe diameters $\chi = 4.75 - 7.13$, mean normalized splash crown heights are generally in the range $\gamma/D_s = 1.0 - 1.6$, approaching the unbounded entry condition. Thus, our results demonstrate that stronger

confinement $\mathcal{C}$ produces substantially taller splash crowns, while differences associated with cross-sectional geometry $\mathcal{G}$ become comparatively less pronounced as the sphere-to-wall separation increases.

Further scrutiny of normalized splash crown heights reveals trends consistent with the results of Watson *et al.*[25], where crown heights exhibit a stronger dependence on Froude number under increased confinement. For cavity-producing impactors traversing confined channels, we expect

$$\frac{\gamma}{D_\mathrm{s}} \sim Fr^{\zeta} \tag{14}$$

to approach linearity, corresponding to $\zeta = 1$, for pipes of arbitrary cross-sectional geometry. We fit this scaling relationship to the experimental data in **Fig.2**c and obtain correlation coefficients in the range $\mathrm{R}^2 = 0.01 - 0.88$ for $\zeta = 1$, with corresponding best fit exponents in the range $\zeta = -0.22 - 1.12$. Consistent with Watson *et al.*[25], normalized splash crown heights γ/D_s exhibit a weak dependence on Fr for unbounded impacts, whereas the strength of the linear dependence generally increases with confinement magnitude across tested geometries. This trend is particularly evident at $\chi = 2.38$, where $\mathrm{R}^2 = 0.88$, 0.79, 0.79, and 0.80 for circular, triangular, square, and hexagonal geometries, respectively. The weak Froude number dependence observed for unbounded impacts, together with the departure of the best fit exponents ζ from unity, may be attributed in part to experimental sensitivity[6], as splash crown heights are known to exhibit substantial trial-to-trial variability even for perfectly spherical projectiles.

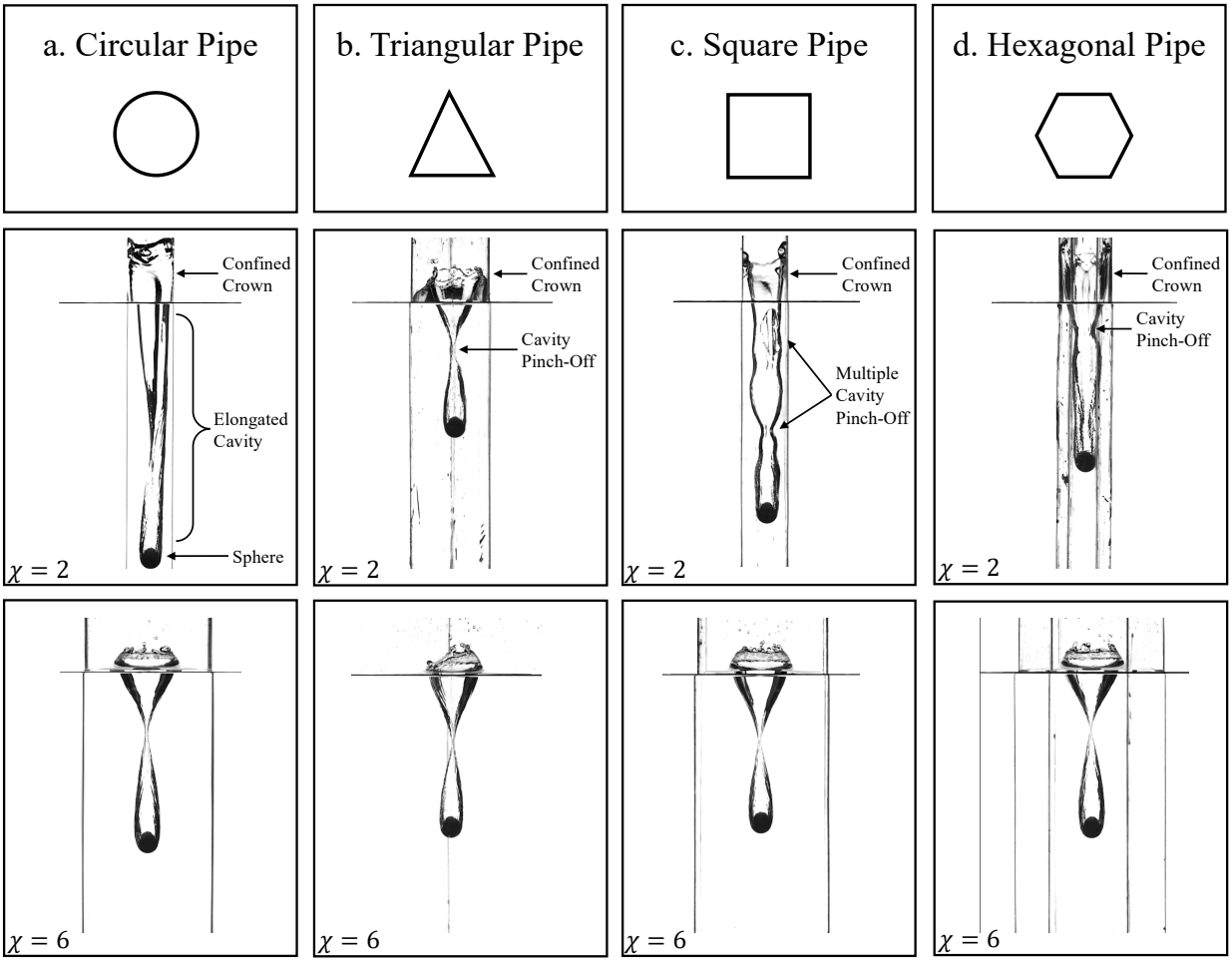


Figure 3: Splash crown and cavity formation during water entry of hydrophobic spheres through **(a)** circular, **(b)** triangular, **(c)** square, and **(d)** hexagonal pipes for strong $\chi = 2$ and weak $\chi = 6$ confinement. Impacting spheres have diameter $D_{\mathrm{s},2} = 1.90$ cm and impacts captured just before cavity pinch-off for Fr = 32.

3.2 Cross-sectional geometry promotes auxiliary cavity dynamics

Cavity evolution provides direct visual evidence that confinement magnitude $\mathcal{C}$ governs water entry through pipes with arbitrary cross-sectional geometry $\mathcal{G}$. **Fig.3** reveals a pronounced transition in cavity morphology with increasing normalized pipe diameter χ, from elongated, strongly confined cavities to shapes that progressively approach the unbounded entry condition. The effect is most evident at $\chi = 2$, where the restricted lateral clearance produces substantially elongated cavities and promotes the onset of multiple pinch-off locations along the cavity length, indicating a marked deviation from the collapse behavior observed under weaker confinement. Increasing χ progressively relaxes these geometric constraints, with cavity morphology at $\chi = 6$ exhibiting a substantially closer resemblance to the unbounded entry condition. These observations establish a clear morphological progression in which confinement magnitude initially dominates cavity evolution, while sufficiently large normalized pipe diameters recover the characteristic cavity structure of an effectively unbounded water entry event. Supplementary movies for circular – movie 1, triangular – movie 2, square – movie 3, and hexagonal pipes – movie 4, provide the corresponding temporal evolution of cavities from impact through collapse and pinch-off.

The effect of confinement magnitude on cavity dynamics is shown in **Fig.4** through the normalized cavity depths κ/D_s. Cavities exhibit greater variation among pipe geometries than splash crowns, particularly at the strongest confinement $\chi = 2$. For the unbounded entry condition $\chi = \infty$, mean cavity depths κ/D_s are 4.78 and 4.24 for the 1.60− and 1.90−cm spheres, respectively, as tabulated in **Table 5**. For $\chi = 2$, mean cavity depth increases to 7.09 for the circular pipe and 8.14 for the hexagonal pipe, while the triangular and square geometries yield smaller values of 3.30 and 5.79, respectively. The circular geometry also exhibits a relatively large normalized cavity depth of 9.64 at $\chi = 2.38$. Corresponding standard deviations σ_{std} are larger than those measured for normalized splash crown widths and heights, reaching 4.69 for the circular pipe at $\chi = 2$ and 4.04 for the hexagonal pipe at $\chi = 2.38$, indicating greater variability in cavity measurements under strong confinement. For intermediate and weak confinement, normalized cavity depths κ/D_s become more closely aligned across the four cross-sectional geometries. For $\chi = 4$, mean values range from 3.20 for the triangular pipe to 4.72 for the circular pipe. At $\chi = 4.75$, the corresponding range decreases to $\kappa/D_s = 2.84 - 4.22$, while values at $\chi = 6$ and 7.13 remain predominantly in the range $\kappa/D_s = 3.4 - 4.1$. Thus, although cavity dynamics exhibit geometry-dependent variations at small χ, the four geometries produce comparatively similar cavity depths as confinement magnitude is relaxed. Convergence toward unbounded cavity depths at larger normalized pipe diameters further indicates that confinement magnitude $\mathcal{C}$ provides the dominant influence on cavity dynamics, with cross-sectional geometry $\mathcal{G}$ producing secondary modifications that are most apparent under strong confinement.

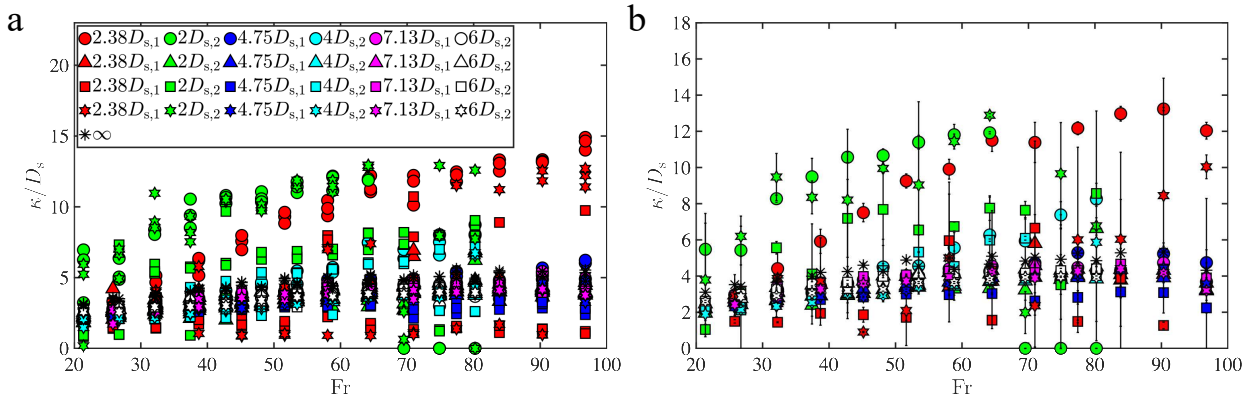


Figure 4: Aggregated plots of normalized cavity depths κ/D_s showing **(a)** replicate tests and **(b)** average values with error bars vs Froude number. Marker shapes visually denote tested cross-sectional geometries $\mathcal{G}$. Mean, standard deviation, and curve fitting values corresponding to linear and best fit predictions are tabulated in **Table 5**.

Cavity measurements also reveal that the influence of Froude number depends strongly on confinement magnitude. Considering previously derived scaling for unbounded, cavity-producing impactors[25], we may

Table 5: Mean, standard deviation, and curve fitting correlation values for normalized cavity depths κ/D_{s} with respect to Froude number ($N = 36$).

Pipe geometry, $\mathcal{G}$	Normalized pipe diameter, χ	Mean	Standard dev., σ_{std}	Best fit R^2, $\zeta = 1$	Best fit exponent, ζ
Circular	2.00	7.09	4.69	0.15	-0.28
	2.38	9.64	3.64	0.94	0.95
	4.00	4.72	2.04	0.86	1.14
	4.75	4.22	0.95	0.82	0.53
	6.00	3.54	0.71	0.67	0.42
	7.13	4.03	0.73	0.58	0.36
Triangular	2.00	3.30	1.23	0.62	0.82
	2.38	3.67	0.93	0.24	0.32
	4.00	3.20	0.55	0.95	0.43
	4.75	3.53	0.52	0.80	0.34
	6.00	3.76	0.64	0.82	0.39
	7.13	3.97	0.57	0.72	0.32
Square	2.00	5.79	2.79	0.26	0.62
	2.38	2.77	2.79	0.04	0.54
	4.00	3.94	1.79	0.34	0.67
	4.75	2.84	0.28	0.13	0.10
	6.00	3.75	0.57	0.81	0.35
	7.13	4.08	0.54	0.74	0.29
Hexagonal	2.00	8.14	3.83	0.02	0.21
	2.38	4.81	4.04	0.31	1.91
	4.00	3.25	1.10	0.75	0.80
	4.75	3.50	0.78	0.86	0.53
	6.00	3.40	0.47	0.92	0.34
	7.13	3.72	0.64	0.60	0.35
∞ ($D_{\mathrm{s}} = 1.60$ cm)	∞	4.78	0.60	0.76	0.28
∞ ($D_{\mathrm{s}} = 1.90$ cm)	∞	4.24	0.58	0.89	0.33

write

$$\frac{\kappa}{D_{\mathrm{s}}} \sim \mathrm{Fr}^{\zeta}. \tag{15}$$

Using Eq.(15), we obtain correlation values in the range $\mathrm{R}^2 = 0.02 - 0.95$ for the linear case $\zeta = 1$, with corresponding best fit exponents in the range $\zeta = -0.28 - 1.91$, as summarized in **Table 5**. The strongest linear relationships occur for several intermediate and weakly confined conditions, including the circular pipe: $\chi = 2.38$, $\mathrm{R}^2 = 0.94$; triangular pipe: $\chi = 4.00$, $\mathrm{R}^2 = 0.95$; and hexagonal pipe: $\chi = 6.00$, $\mathrm{R}^2 = 0.92$.

In contrast, several of the most strongly confined configurations exhibit substantially weaker dependence on Fr, including the circular and hexagonal geometries at $\chi = 2.00$, for which $R^2 = 0.15$ and 0.02, respectively. These results indicate that, although impact inertia remains an important control on normalized cavity depths κ/D_s, its influence becomes less systematic under strong confinement, where cavity dynamics is increasingly governed by the surrounding boundary. The comparatively strong Froude number dependence recovered for the unbounded entry condition, with $R^2 = 0.76$ and 0.89 for the two sphere diameters, $D_{s,1}$ and $D_{s,2}$, respectively, further supports this interpretation. Thus, weakening of the relationship shown in Eq.(15) under the strongest confinement suggests that pipe diameter increasingly supersedes impact conditions in governing cavity development.

Collectively, these results demonstrate that cavity dynamics reflect a competition between impact inertia and geometric confinement. Although Froude number remains an important control on normalized cavity depths κ/D_s, the increasingly variable scaling observed under strong confinement indicates that the surrounding boundary exerts a progressively greater influence on cavity development. As confinement is relaxed, normalized cavity depths across the four geometries converge toward the unbounded response, reinforcing the conclusion that confinement magnitude provides the primary control, while cross-sectional geometry acts as an auxiliary modifier of the resulting cavity dynamics.

3.3 Geometric confinement controls hydrodynamic loading

The influence of confinement on sphere kinematics is illustrated in **Fig.5**a, where we present normalized vertical position y/D_s, as a function of normalized time Ut/D_s, for a 1.90−cm sphere with impact velocity $U = 2.43$ m/s. Sphere motion is tracked from the instant the sphere crosses the undisturbed free surface, defined by $y = 0$, until immediately before it reaches the aquarium floor. Throughout the submerged trajectory, spheres remain aligned with the vertical centerline of pipes, with no appreciable lateral displacement observed following impact. This behavior is consistent across the investigated confinement magnitudes and cross-sectional geometries. Consequently, present analysis is restricted to the spheres' vertical displacement and a corresponding force balance adopted from Watson *et al.*[25] is employed. Thus,

$$\frac{du}{dt} = \frac{mg}{m'} - \frac{\rho g \pi D^2}{8m'}\left(\frac{4D}{3} + 2y + \frac{C_D u^2}{g}\right), \tag{16}$$

where $m' = m + m_a$ is the effective sphere mass and $m_a = \pi\rho D^3 C_m/6$ is the added mass associated with acceleration of the surrounding liquid. The added-mass coefficient is taken as $C_m = 0.5$ for all experimental conditions. Although C_m evolves from zero as the sphere initially penetrates the free surface, Watson *et al.*[3] demonstrated that the resulting force model is comparatively insensitive to this transient variation when $m/m_a \sim O(10)$. Sphere kinematics are obtained from measured vertical position $y(t)$ exported from Open-Source Physics Tracker. Prior to numerical differentiation, position measurements are processed in MATLAB® using a Savitzky–Golay filter to suppress experimental noise that would otherwise be amplified by numerical differentiation. Filtered position signal is differentiated to obtain instantaneous velocity $u(t)$, after which the resulting velocity measurements are filtered again and numerically differentiated to determine instantaneous acceleration $a(t)$. The Savitzky–Golay procedure locally approximates the measured data using polynomial least-squares regression, thereby reducing high-frequency measurement fluctuations while preserving the underlying temporal variation of the sphere trajectory. This processing methodology follows the approach previously validated by Watson *et al.*[25] and is used here to minimize nonphysical artifacts introduced during numerical differentiation.

Sphere trajectories demonstrate measurable differences in descent among the confined configurations, indicating that the surrounding boundaries modify the resistance experienced by the sphere during its underwater motion. Relative to the unbounded trajectory, confined cases exhibit greater deceleration, with the magnitude of the departure increasing as the available cross-sectional area is reduced. This behavior is consistent with confinement-dependent changes observed in splash and cavity measurements, where the strongest modifications likewise occur at the smallest normalized pipe diameters. The corresponding hydrodynamic drag coefficients C_D, are shown in **Fig.5**b as a function of instantaneous Reynolds number $Re = \rho D_s u(t)/\mu = 42,000 - 53,000$. Confined configurations exhibit increased hydrodynamic resistance relative to the unbounded entry condition over the measured Reynolds number range. Mean hydrodynamic drag coefficients ($N = 149$) for the circular, triangular, square, and hexagonal configurations are

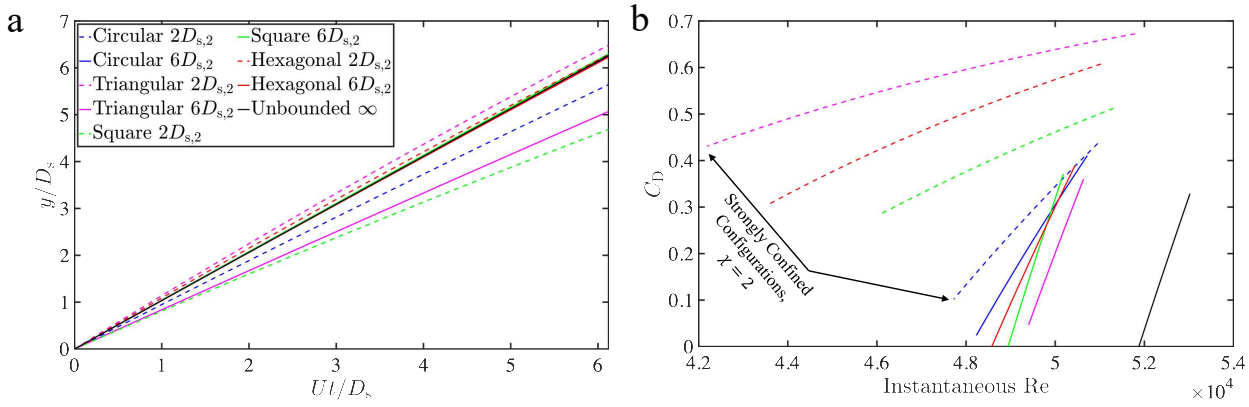


Figure 5: **(a)** Normalized vertical position y/D_s vs normalized time Ut/D_s. **(b)** Hydrodynamic drag coefficient C_D vs instantaneous Reynolds number Re.

$C_{\mathrm{D,avg}} = 0.28 \pm 0.10$, 0.57 ± 0.07, 0.40 ± 0.07, and 0.47 ± 0.09, respectively, at $\chi = 2$, decreasing to $C_{\mathrm{D,avg}} = 0.22 \pm 0.11$, 0.21 ± 0.09, 0.17 ± 0.12, and 0.20 ± 0.11 at $\chi = 6$, compared with $C_{\mathrm{D,avg}} = 0.15 \pm 0.10$ for the unbounded condition. Despite differences among cross-sectional geometries, the principal change is associated with the introduction of the surrounding boundary, while the variation between geometries is comparatively smaller. Drag measurements therefore align with the overall trend identified for splash crowns and cavities: decreasing χ produces a stronger modification of water entry dynamics, whereas increasing χ reduces the influence of the pipe boundary. Together, the trajectories and drag measurements demonstrate that confinement magnitude affects not only the free-surface morphology but also the hydrodynamic loading and subsequent deceleration of descending spheres.

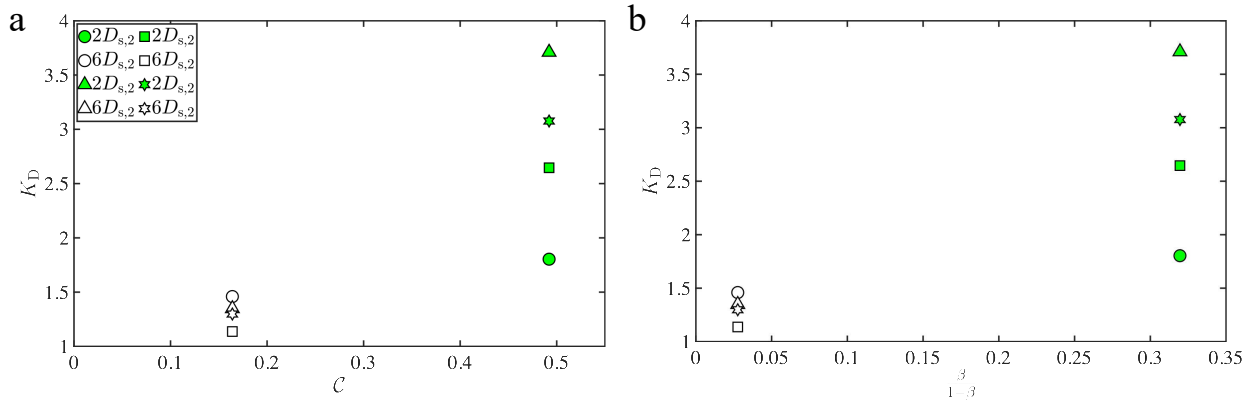


Figure 6: Drag augmentation factor $K_\mathrm{D} = C_\mathrm{D}/C_{\mathrm{D},\infty}$ as a function of **(a)** confinement magnitude $\mathcal{C}$ and **(b)** a blockage-based parameter $\beta/1-\beta$. Filled and open markers denote the strongly $\chi = 2$ and weakly $\chi = 6$ confined conditions, respectively, while marker shape identifies pipe cross-sectional geometry.

To further examine the geometric dependence of hydrodynamic loading, we define the drag augmentation factor

$$K_\mathrm{D} = \frac{C_{\mathrm{D,avg}}}{C_{\mathrm{D},\infty}}, \tag{17}$$

where $C_{\mathrm{D},\infty}$ is the mean drag coefficient for the unbounded entry condition. **Fig.6** compares K_D using confinement magnitude $\mathcal{C} = 1/\chi$ and the blockage-based parameter $\beta/1-\beta$. The latter represents the ratio of the projected sphere area to the remaining cross-sectional area available for fluid redistribution and

follows naturally from the continuity scaling derived in Section 2. Both representations reveal a pronounced increase in hydrodynamic resistance with increasing confinement. For the more weakly confined conditions, K_D remains comparatively close to unity, with values of approximately $1.1 - 1.5$, and differences among cross-sectional geometries are relatively small. Strong confinement produces substantially larger values, $K_D \approx 1.8 - 3.7$, together with a marked increase in the variation among pipe geometries. Importantly, recasting confinement in terms of $\beta/1 - \beta$ does not eliminate this geometry-dependent variation. Thus, although blockage provides a physically relevant measure of the restriction imposed on sphere-induced fluid displacement, hydrodynamic loading cannot be described by available cross-sectional area alone.

The persistence of geometry-dependent differences under strong confinement indicates that the spatial distribution of the surrounding boundary becomes increasingly important as the sphere approaches pipe walls. Pipes having comparable characteristic confinement can differ substantially in their local wall separation and corner regions, thereby providing distinct pathways for fluid redistribution around descending spheres. Our results therefore support a hierarchy in which confinement magnitude $\mathcal{C}$ establishes the overall increase in hydrodynamic resistance, while cross-sectional geometry $\mathcal{G}$ determines an increasingly significant correction in the strongly confined regime.

4 Discussion

Our experiments reveal a consistent hierarchy of geometric effects in confined water entry. Confinement magnitude, quantified as $\mathcal{C} = 1/\chi$, provides the leading modification to splash crown formation, cavity dynamics, and hydrodynamic loading, whereas cross-sectional geometry produces comparatively smaller departures at equivalent pipe diameters. Across all tested governing parameters, the influence of pipe shape becomes most prominent under strong confinement and progressively diminishes as the surrounding boundary is displaced farther from the sphere. This behavior indicates that the principal role of the pipe is to restrict fluid motion generated by sphere entry, while detailed boundary geometry modifies how that restricted flow is spatially redistributed.

Splash crown measurements provide one manifestation of this hierarchy. Strong confinement produces the greatest deviation from unbounded splash crown behavior, while relaxation of confinement causes the changes associated with different pipe geometries to become increasingly similar. Reduced sensitivity to cross-sectional shape at larger normalized pipe diameters is consistent with a progressive weakening of wall-induced constraints on the radial motion of displaced liquid. Under strong confinement, however, noncircular boundaries introduce spatial variations in sphere-to-wall distance that can alter the local redistribution of liquid near the free surface, thereby producing measurable differences in both splash crown width and height. Cross-sectional geometry therefore appears to modify a free-surface response whose overall magnitude is established primarily by confinement magnitude.

Cavities exhibit stronger sensitivity to cross-sectional geometry than splash crowns. This distinction is physically reasonable since the cavity forms an extended air-filled structure that interacts with the surrounding liquid and boundary over a substantially greater vertical extent than the initial splash crown. Polygonal pipes introduce nonuniform wall proximity around the cavity perimeter, allowing local collapse to proceed differently depending on the instantaneous cavity shape and its position relative to pipe faces and corners. These effects can modify cavity symmetry, collapse location, and pinch-off behavior, particularly in the strongly confined regime. As confinement is relaxed, these local boundary effects weaken and cavity depths become more consistent among different geometries. The results therefore suggest that cross-sectional geometry is most important for the detailed morphology and collapse dynamics of the cavity rather than for establishing the overall strength of confinement.

Hydrodynamic loading provides a complementary dynamical interpretation of the same confinement process. Confined spheres decelerate more strongly when compared to unbounded water entry, and corresponding drag coefficients increase as the available fluid region surrounding the sphere is restricted. This increase in resistance is consistent with the need to redirect sphere-displaced liquid through a reduced cross-sectional area. The resulting increase in characteristic fluid velocity and pressure provides a common physical basis for the observed changes in sphere deceleration, splash crown formation, and cavity behavior. These water entry dynamics should therefore be viewed as coupled consequences of the interaction between sphere-induced flow and the surrounding boundary rather than as independent confinement effects. Our

drag augmentation analysis further clarifies this interpretation. Both the confinement magnitude $\mathcal{C}$ and the blockage-based parameter $\beta/1-\beta$ capture the overall increase in hydrodynamic resistance as confinement strengthens, but neither eliminates the variation among pipe geometries in the strongly confined regime. This persistence indicates that available cross-sectional area alone does not fully characterize the confined flow. Instead, local wall separation, corner regions, and the nonuniform distribution of the surrounding boundary provide additional geometric influences on fluid redistribution. Confinement magnitude therefore establishes the dominant increase in hydrodynamic resistance, while detailed cross-sectional geometry becomes an increasingly important correction as the sphere approaches pipe walls.

These findings extend previous investigations[25] of circular confinement by showing that the principal wall-induced trends observed for circular pipes persist for triangular, square, and hexagonal boundaries. Confined water entry across the present geometries can therefore be organized using a common confinement parameter, while responses associated with cross-sectional shape become increasingly relevant in the near-wall limit. This distinction is useful because it suggests that noncircular boundaries need not be treated as entirely separate confinement regimes; instead, their influence may be interpreted as a geometry-dependent modification to a response that is primarily established by the confinement magnitude. Notwithstanding, the present interpretation remains limited to the experimental parameter space considered here. Pipes were compared using a common inscribed diameter, which provides a consistent measure of minimum wall-to-wall dimension and hydraulic diameter but does not produce identical cross-sectional areas or wall-distance distributions. Consequently, residual geometry effects observed under strong confinement likely reflect contributions from both local wall placement and the redistribution of available flow area. Experiments are also restricted to hydrophobic spheres, a limited range of Froude numbers, two sphere diameters, and the circular and regular polygonal cross-sections considered here. The conclusions should therefore be interpreted as establishing a hierarchy within the present parameter range rather than as demonstrating universal geometry-independent behavior.

Overall, measurements support a first-order description in which normalized pipe diameter characterizes the dominant confinement effect, while cross-sectional geometry governs secondary spatial features that become increasingly significant under strong confinement. Such a framework provides a practical basis for comparing water entry through pipes of different shapes while retaining geometric detail when cavity morphology, local flow redistribution, or hydrodynamic loading in the strongly confined regime is of specific interest.

5 Conclusion

Hydrophobic sphere water entry through circular, triangular, square, and hexagonal pipes was examined to determine the relative importance of confinement magnitude and cross-sectional geometry. Across the tested experimental conditions, confinement magnitude produced systematic changes in splash crown formation, cavity dynamics, and hydrodynamic loading, while differences associated with cross-sectional shape became progressively more important as spheres approached the surrounding boundary. These observations establish a clear hierarchy in which confinement magnitude governs water entry and cross-sectional geometry provides a secondary, increasingly significant correction under strong confinement. The common inscribed diameter used to characterize tested pipes is also their hydraulic diameter, providing a consistent length scale for comparison across geometries. However, equal hydraulic diameters do not imply equal cross-sectional flow areas or identical wall-distance distributions. Our blockage analysis showed that restriction of the available flow area contributes to an increase in hydrodynamic resistance, but does not alone account for the geometry-dependent variations observed under strong confinement. Confined water entry therefore reflects both the overall restriction imposed on sphere-induced fluid displacement and the detailed spatial arrangement of the surrounding boundary. Measurements indicate that normalized pipe diameter provides a useful first-order parameter for organizing confined water entry across the geometries examined here. Cross-sectional geometry becomes most relevant when local cavity morphology, flow redistribution, and hydrodynamic loading are strongly influenced by nearby pipe walls and corner regions. Future studies incorporating additional geometries, stronger confinement, and direct three-dimensional measurements of the surrounding flow field would help establish the limits of this confinement hierarchy and identify local mechanisms responsible for the remaining geometry-dependent effects.

Acknowledgements

We would like to acknowledge the Florida Polytechnic University for partial support.

Declaration of Interests

The authors report no conflict of interest.

Data Availability

The data that support the findings of this study are available from the corresponding author upon reasonable request.

References

[1] Watson, D. A., Stephen, J. L. & Dickerson, A. K., 2018 Jet amplification and cavity formation induced by penetrable fabrics in hydrophilic sphere entry. *Physics of Fluids* **30**, 082109. (doi:10.1063/1.5036655).

[2] Watson, D. A., Stephen, J. L. & Dickerson, A. K., 2019 Impacts of free-falling spheres onto a deep liquid pool with altered fluid and impactor surface conditions. *Journal of Visualized Experiments* **144**, e59300. (doi:10.3791/59300).

[3] Watson, D. A., Souchik, C. J., Weinberg, M. P., Bom, J. M. & Dickerson, A. K., 2020 Making a splash with fabrics in hydrophilic sphere entry. *Journal of Fluids and Structures* **94**, 102907. ISSN 0889-9746. (doi:10.1016/j.jfluidstructs.2020.102907).

[4] Watson, D. A., Bom, J. M., Weinberg, M. P., Souchik, C. J. & Dickerson, A. K., 2021 Water entry dynamics of spheres with heterogeneous wetting properties. *Physical Review Fluids* **6**, 044003. (doi: 10.1103/PhysRevFluids.6.044003).

[5] Akbarzadeh, P., Krieger, M., Hofer, D., Thumfart, M. & Gittler, P., 2023 Parallel water entry: Experimental investigations of hydrophobic/hydrophilic spheres. *Physics of Fluids* **35**, 103301. ISSN 1070-6631. (doi:10.1063/5.0167494).

[6] Watson, D. A., Anzola, S., Zeas, F. A., Smith, K. B. & Cruz, A. A., 2024 Compound cavity formation and splash crown suppression by water entry through proximally adjacent polystyrene beads. *Physics of Fluids* **36**, 092124. ISSN 1070-6631. (doi:10.1063/5.0226769).

[7] Aristoff, J. M., Truscott, T. T., Techet, A. H. & Bush, J. W. M., 2008 The water entry cavity formed by low bond number impacts. *Physics of Fluids* **20**, 091111. (doi:10.1063/1.2973662).

[8] Aristoff, J. & Bush, J., 2009 Water entry of small hydrophobic spheres. *Journal of Fluid Mechanics* **619**, 45 – 78. ISSN 00221120. (doi:10.1017/S0022112008004382).

[9] Aristoff, J., Truscott, T., Techet, A. & Bush, J., 2010 The water entry of decelerating spheres. *Physics of Fluids* **22**. ISSN 10706631. (doi:10.1063/1.3309454).

[10] Duez, C., Ybert, C., Clanet, C. & Bocquet, L., 2007 Making a splash with water repellency. *Nature Physics* **3**, 180 – 183. ISSN 17452473. (doi:10.1038/nphys545).

[11] Li, D., Zhang, J., Zhang, M., Huang, B., Ma, X. & Wang, G., 2019 Experimental study on water entry of spheres with different surface wettability. *Ocean Engineering* **187**, 106123. ISSN 0029-8018. (doi:10.1016/j.oceaneng.2019.106123).

[12] Truscott, T. T., Epps, B. P. & Belden, J., 2013 Water entry of projectiles. *Annual Review of Fluid Mechanics* **46**, 355 – 378. ISSN 00664189. (doi:10.1146/annurev-fluid-011212-140753).

[13] Duclaux, V., Caille, F., Duez, C., Ybert, C., Bocquet, L. & Clanet, C., 2007 Dynamics of transient cavities. *Journal of Fluid Mechanics* **591**. ISSN 1469-7645. (doi:10.1017/s0022112007007343).

[14] Kubota, Y. & Mochizuki, O., 2011 Influence of head shape of solid body plunging into water on splash formation. *Journal of Visualization* **14**, 111–119. ISSN 1875-8975. (doi:10.1007/s12650-011-0071-4).

[15] Bodily, K. G., Carlson, S. J. & Truscott, T. T., 2014 The water entry of slender axisymmetric bodies. *Physics of Fluids* **26**, 072108. ISSN 1089-7666. (doi:10.1063/1.4890832).

[16] Worthington, A. M. & Cole, R. S., 1897 Impact with a liquid surface studied by the aid of instantaneous photography. *Philosophical Transactions of the Royal Society of London. Series A, Containing Papers of a Mathematical or Physical Character* **189**, 137–148. ISSN 0264-3952. (doi:10.1098/rsta.1897.0005).

[17] Worthington, A. M. & Cole, R. S., 1900 Impact with a liquid surface studied by the aid of instantaneous photography. paper ii. *Philosophical Transactions of the Royal Society of London. Series A, Containing Papers of a Mathematical or Physical Character* **65**, 153–154. ISSN 0370-1662. (doi:10.1098/rspl.1899.0014).

[18] Worthington, A. M., 1908 *A study of splashes*. Longmans, Green, and Co. (doi:10.1126/science.29.742.46).

[19] Ern, P. & Brosse, N., 2014 Interaction of two axisymmetric bodies falling side by side at moderate reynolds numbers. *Journal of Fluid Mechanics* **741**, R6. (doi:10.1017/jfm.2013.683).

[20] Lu, L., Wang, C., Li, Q. & Sahoo, P. K., 2021 Numerical investigation of water-entry characteristics of high-speed parallel projectiles. *International Journal of Naval Architecture and Ocean Engineering* **13**, 450–465. ISSN 2092-6782. (doi:10.1016/j.ijnaoe.2021.05.003).

[21] Wang, X., Lyu, X., Sun, R. & Tang, D., 2024 Numerical study on the cavity dynamics for vertical water entries of twin spheres. *Defence Technology* **32**, 459–472. ISSN 2214-9147. (doi:10.1016/j.dt.2023.02.020).

[22] Akbarzadeh, P., Krieger, M., Hofer, D., Thumfart, M. & Gittler, P., 2025 Parallel water entry of hydrophobic-hydrophilic sphere pairings: particle image velocimetry and high-speed camera analysis. *Journal of Fluids and Structures* **133**, 104272. ISSN 0889-9746. (doi:10.1016/j.jfluidstructs.2025.104272).

[23] Zeng, L., Balachandar, S. & Fischer, P., 2005 Wall-induced forces on a rigid sphere at finite reynolds number. *Journal of Fluid Mechanics* **536**, 1–25. (doi:10.1017/S0022112005004738).

[24] Mansoor, M. M., Marston, J. O., Vakarelski, I. U. & Thoroddsen, S. T., 2014 Water entry without surface seal: extended cavity formation. *Journal of Fluid Mechanics* **743**, 295–326. (doi:10.1017/jfm.2014.35).

[25] Watson, D. A., Joseph, Z. C., Vidana-Fuentes, D. A., Anzola, S. & Zeas, F. A., 2025 Water entry dynamics of hydrophobic spheres bounded by semi-infinite cylindrical pipes. *Physics of Fluids* **37**, 112115. ISSN 1070-6631. (doi:10.1063/5.0300541).

[26] Ali, S. H., Al-Zuky, A. A. D., Al-Saleh, A. H. & Mohamad, H. J., 2019 Measure liquid viscosity by tracking falling ball automatically depending on image processing algorithm. *Journal of Physics: Conference Series* **1294**, 022002. (doi:10.1088/1742-6596/1294/2/022002).

[27] Isken, M. W. & Littig, S. J., 2002 Simulation analysis of pneumatic tube systems. *Journal of Medical Systems* **26**, 9–19. (doi:10.1023/a:1013034719088).

[28] Kapoula, G. V., Kontou, P. I. & Bagos, P. G., 2017 The impact of pneumatic tube system on routine laboratory parameters: a systematic review and meta-analysis. *Clinical Chemistry and Laboratory Medicine* **55**, 1834–1844. (doi:10.1515/cclm-2017-0008).

[29] Shin, J. & McMahon, T. A., 1990 The tuning of a splash. *Physics of Fluids A: Fluid Dynamics* **2**, 1312–1317. (doi:10.1063/1.857581).